43rd AIAA/ASME/SAE/ASEE Joint Propulsion Conference & Exhibit
8 - 11 July 2007, Cincinnati, OH

AIAA 2007-5797

Energy Steepened States of the Taylor-Culick Profile

Joseph Majdalani* and Tony Saad†
University of Tennessee Space Institute, Tullahoma, TN 37388

The Taylor-Culick solution for a porous cylinder has long been used to describe the bulk gas motion in idealized representations of solid rocket motors. By superimposing an arbitrary headwall injection velocity, a modified form of this solution can be extended to hybrid rocket applications and to solids with reactive headwall. However, the Taylor-Culick solution appears not to be unique for a prescribed set of boundary conditions. Other solutions may be found that satisfy the same fundamental constraints. As alluded to in the literature, steeper or smoother profiles can be observed in both experimental and numerical tests, particularly in the presence of intense levels of acoustic energy. In this study, we present the system of equations that leads to multiple solutions. We then search for the extreme states that require the least or the most kinetic energy. These solutions are derived and found to be dependent on the chamber aspect ratio and the headwall injection profile. They are evaluated for several baseline cases and compared to numerical simulations. By assuming a sufficiently large aspect ratio, simple expressions are obtained over a finite range of kinetic energies. Some exhibit steep, turbulent-like features that confirm the experimental and numerical findings by CSAR, ATK Thiokol, and ONERA investigators who have often reported steeper profiles than predicted by Taylor-Culick's basic cold flow model. The solutions presented here are quasi-viscous, specifically in their ability to secure the no slip condition at the sidewall. They are evaluated for several headwall injection patterns and cataloged based on their kinetic energies. In practice, the steepening/dampening process can be sustained through acoustic energy buildup and release, a common occurrence in rocket chambers. In this vein, the advent of energy-sensitive mean flow solutions enables us to conceptualize a two-way coupling theory connecting the mean flow to the unsteady wave motion.

Nomenclature

a	= chamber radius
r, z	= normalized radial and axial coordinate, $\bar{r}/a$, $\bar{z}/a$
$\boldsymbol{u}$	= normalized velocity $(\bar{u}_r, \bar{u}_z)/U_w$
U_c	= headwall injection velocity, $\bar{u}_z(0,0)$
u_c	= normalized injection velocity, U_c/U_w
U_w	= sidewall injection velocity, $-\bar{u}_r(a,\bar{z})$
η	= action variable, $\frac{1}{2}\pi(2n+1)r^2$
ν	= kinematic viscosity, μ/ρ
ρ	= density

Subscripts and Symbols

c	= centerline property
h	= headwall property
r, z	= radial and axial component or partial derivative
w	= sidewall property
$\bar{\ }$	= overbars denote dimensional variables

*Jack D. Whitfield Professor of High Speed Flows, Department of Mechanical, Aerospace and Biomedical Engineering. Member AIAA. Fellow ASME.
†Doctoral Research Assistant, Department of Mechanical, Aerospace and Biomedical Engineering. Member AIAA.

I. Introduction

IT may be argued that the Taylor-Culick model for approximating the internal flowfield in solid rocket motors stands at the foundation of a host of theoretical problems that are of fundamental interest to the propulsion community.[1] For example, in the study of aeroacoustic instability,[2-4] it has provided a mean flow approximation about which fluctuations may be induced.[5] In studying the effect of particle addition and particle-mean flow interactions, it has fallen at the epicenter of hydrodynamic instability theory.[6,7] In large-scale numerical simulations that involve particle burning and agglomeration, average speeds and accelerations within the chamber have routinely been estimated directly from the Taylor-Culick solution. One may refer in this regard to the work of Najjar *et al.*,[8,9] Balachandar, Buckmaster and Short,[10] as well as others. In reactive flow simulations, the Taylor-Culick solution is so valuable in estimating the bulk gas motion that it has been either built into the codes or used as a benchmark to verify computations. This is illustrated by Chu, Yang and Majdalani[11] in their premixed propane-air simulation of solid propellant burning, and by Chedevergne, Casalis and Majdalani[12] in their DNS simulations of an idealized solid rocket motor (SRM).

The basic Taylor-Culick solution is incompressible, rotational, axisymmetric, and quasi-viscous.[13] It has been extended by Majdalani and co-workers to account for viscous stresses and regressing walls,[14] and, subsequently, for arbitrary headwall mass addition.[15] By permitting variable headwall injection profiles, the extended Taylor-Culick approximation can be a viable model for idealized hybrid rocket chambers.[15-17] Its accuracy has been verified in several investigations including computational,[18-20] experimental,[20-22] and theoretical pursuits carried out in both cylindrical[14] and planar (slab) configurations.[23,24] Recently, it has been extended to noncircular cross-sections by Kurdyumov.[25] It is clearly one of the most ubiquitous cold flow approximations for a full-length cylindrical motor.[26] This is especially true in applications that require an analytical mean flow formulation; examples abound, and one may cite those studies concerned with vortico-acoustic wave propagation[5] and hydrodynamic instability treatment in porous chambers with[6,7] and without particle interactions.[27-33] The compressible Taylor-Culick solution has also been developed under compressible isentropic flow conditions by Majdalani.[34]

In this study, we revisit the procedure leading to the Taylor-Culick incompressible model. In the process, we construct multiple approximate solutions that will satisfy the problem's constraints. Among those, we apply the energy optimization principle to identify the particular forms that require the most or the least kinetic energy to be manifested. The bracketing solutions are determined and cataloged for several headwall injection profiles. Solutions are then compared and classified according to their energy signature. In all cases, simple approximations are obtained assuming sufficiently long chambers. These solutions are characterized and discussed.

II. Formulation

The basic rocket chamber can be modeled as a porous cylinder of length L_0 and radius a. We also permit the forward end to be porous while assuming an open aft end. As shown in Fig. 1, $\bar{r}$ and $\bar{z}$ stand for the radial and axial coordinates. Note that the porous headwall permits the injection of a fluid at a prescribed velocity profile, $\bar{u}_0$. Special cases of $\bar{u}_0$ include

$$\bar{u}_0(\bar{r}) = \bar{u}_z(\bar{r},0) = \begin{cases} U_c = \text{const}; & \text{uniform} \\ U_c \cos(\tfrac{1}{2}\pi\bar{r}^2/a^2); & \text{Berman (half cosine)} \\ U_c[1-(\bar{r}/a)^m]; & \text{laminar } (m=2) \text{ and turbulent} \\ U_c(1-\bar{r}/a)^{1/m}; & \text{turbulent } (m=1/7) \end{cases} \tag{1}$$

Our solution domain extends from the headwall to the parallel, virtual nozzle attachment plane at the aft end.

At the headwall, an axial jet enters the chamber at a maximum centerline speed, U_c. This stream is then augmented by uniform mass addition along the porous sidewall. In what follows, we seek to approximate other solutions that may exist besides Taylor-Culick's basic relation. In particular, we hope to identify those particular solutions that require the least or most energy to excite.

A. Equations

An inert flow may be assumed, prompted by the typically thin reactive zone above the grain surface. Following rote, the basic flow can be taken to be steady, inviscid, incompressible, rotational, and axisymmetric. The inviscid equations of motion become

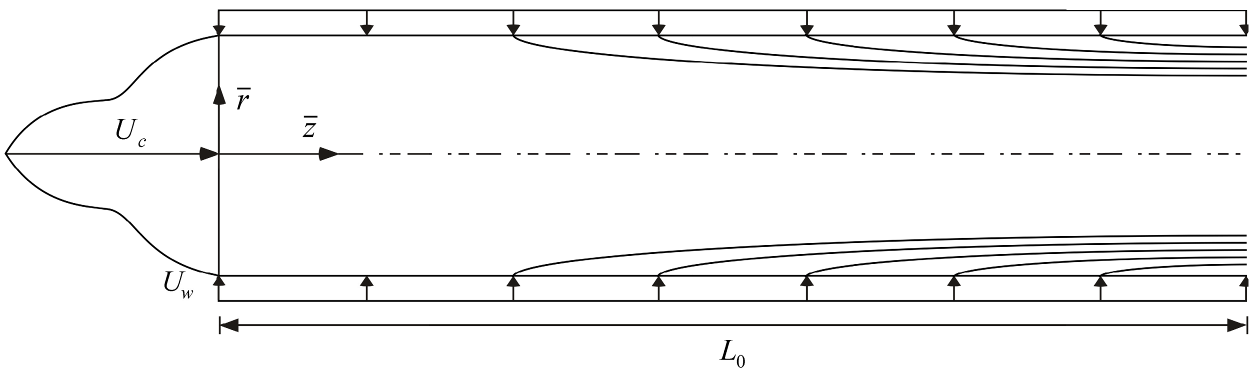

Figure 1. Simulated rocket chamber as a porous cylinder with arbitrary headwall injection.

$$\frac{1}{\bar{r}}\frac{\partial(\bar{r}\bar{u}_r)}{\partial\bar{r}}+\frac{\partial\bar{u}_z}{\partial\bar{z}}=0 \tag{2}$$

$$\bar{u}_r\frac{\partial\bar{u}_r}{\partial\bar{r}}+\bar{u}_z\frac{\partial\bar{u}_r}{\partial\bar{z}}=-\frac{1}{\rho}\frac{\partial\bar{p}}{\partial\bar{r}} \tag{3}$$

$$\bar{u}_r\frac{\partial\bar{u}_z}{\partial\bar{r}}+\bar{u}_z\frac{\partial\bar{u}_z}{\partial\bar{z}}=-\frac{1}{\rho}\frac{\partial\bar{p}}{\partial\bar{z}} \tag{4}$$

B. Boundary Conditions

These are physically connected to

(a) axial symmetry and therefore no flow across the centerline;
(b) vanishing parallel flow at the sidewall to secure the no slip boundary condition;
(c) uniform injection at the cylindrical sidewall; and
(d) a user-prescribed injection pattern at the headwall.

Mathematically, these particulars can be written as

$$\begin{cases} \bar{r}=0,\ 0\le\bar{z}<L_0; & \bar{u}_r=0 \quad \text{(no flow across centerline)} \\ \bar{r}=a,\ 0\le\bar{z}<L_0; & \bar{u}_z=0 \quad \text{(no slip at the wall)} \\ \bar{r}=a,\ 0\le\bar{z}<L_0; & \bar{u}_r=-U_w \quad \text{(sidewall mass addition)} \\ \bar{z}=0,\ 0\le\bar{r}<a; & \bar{u}_z=\bar{u}_0(\bar{r}) \quad \text{(variable headwall injection)} \end{cases} \tag{5}$$

C. Normalization

All recurring variables and operators may be normalized via

$$z=\frac{\bar{z}}{a};\ r=\frac{\bar{r}}{a};\ \nabla=a\bar{\nabla};\ p=\frac{\bar{p}}{\rho U_w^2};\ \psi=\frac{\bar{\psi}}{a^2U_w} \tag{6}$$

$$u_r=\frac{\bar{u}_r}{U_w};\ u_z=\frac{\bar{u}_z}{U_w};\ \boldsymbol{\Omega}=\frac{\bar{\boldsymbol{\Omega}}a}{U_w};\ u_c=\frac{U_c}{U_w};\ L=\frac{L_0}{a} \tag{7}$$

Here $U_c=\bar{u}_z(0,0)$ and $U_w=-\bar{u}_r(a,\bar{z})$ designate the fluid injection velocities at the headwall and sidewall, respectively. For steady inviscid motion, the vorticity transport equation reduces to

$$\nabla\times\boldsymbol{u}\times\boldsymbol{\Omega}=0\,;\quad \boldsymbol{\Omega}=\nabla\times\boldsymbol{u} \tag{8}$$

Similarly, the dimensionless boundary conditions take the form

$$\begin{cases} u_r(0,z)=0 & \text{(no flow across centerline)} \\ u_z(1,z)=0 & \text{(no slip at sidewall)} \\ u_r(1,z)=-1 & \text{(constant radial inflow at sidewall)} \\ u_z(r,0)=u_0(r) & \text{(axial inflow at headwall)} \end{cases} \tag{9}$$

D. Vorticity-Stream Function Approach

The Stokes stream function may be introduced through

$$u_r = -\frac{1}{r}\frac{\partial \psi}{\partial z} \quad \text{and} \quad u_z = \frac{1}{r}\frac{\partial \psi}{\partial r} \tag{10}$$

As usual, substitution into Eq. (8) requires

$$\Omega = \Omega_\theta = rF(\psi) \tag{11}$$

One then follows tradition[13] and selects the simplest relation between Ω and ψ, namely,

$$\Omega = C^2 r\psi \tag{12}$$

Despite the non-uniqueness of this expression, it permits securing Eq. (9). By inserting Eq. (12) into the vorticity equation, one eliminates Ω and restores the PDE characteristic of this problem. This is

$$\frac{\partial^2\psi}{\partial z^2} + \frac{\partial^2\psi}{\partial r^2} - \frac{1}{r}\frac{\partial \psi}{\partial r} + C^2 r^2 \psi = 0 \tag{13}$$

with the particular set of constraints being:

$$\lim_{r\to 0}\frac{1}{r}\frac{\partial \psi(r,z)}{\partial z} = 0 \quad \text{(a);} \quad \frac{\partial \psi(1,z)}{\partial r} = 0 \quad \text{(b);} \quad \frac{1}{r}\frac{\partial \psi(r,z)}{\partial z}\bigg|_{r=1} = 1 \quad \text{(c);} \quad \frac{1}{r}\frac{\partial \psi(r,0)}{\partial r} = u_0(r) \quad \text{(d)} \tag{14}$$

By virtue of L'Hôpital's rule, removing the singularity in Eq. (14)a requires that both

$$\frac{\partial \psi(0,z)}{\partial z} = 0 \quad \text{(a)} \quad \text{and} \quad \frac{\partial^2 \psi(0,z)}{\partial r \partial z} = 0 \quad \text{(b)} \tag{15}$$

Equation (13) is then solved by separation of variables; one finds

$$\psi(r,z) = (\alpha z + \beta)[A\cos(\tfrac{1}{2}Cr^2) + B\sin(\tfrac{1}{2}Cr^2)] \tag{16}$$

This expression satisfies Eq. (15)b identically. So from this point forward, Eq. (14)a may be replaced by Eq. (15)a.

III. Energy Triggered Solutions

A. Solution by Eigenfunction Expansions

The application of the boundary conditions must be carefully carried out, preferably in the order in which they appear. For example, Eq. (15)a gives:

$$\frac{\partial \psi(0,z)}{\partial z} = \alpha A\cos(\tfrac{1}{2}Cr^2) + \alpha B\sin(\tfrac{1}{2}Cr^2)\Big|_{r=0} = 0 \tag{17}$$

or $A = 0$. Without loss in generality, one may set $B = 1$ and rewrite Eq. (14)b as

$$rC(\alpha z + \beta)\cos(\tfrac{1}{2}Cr^2)\Big|_{r=1} = 0; \quad \forall z \tag{18}$$

and so $\cos(\tfrac{1}{2}C) = 0$; this is satisfied by

$$C = C_n = (2n+1)\pi;\ n = \{0,1,2,...,\infty\} \in \mathbb{N} \tag{19}$$

Using $C_n = (2n+1)\pi$ enables us to sum over eigenfunctions corresponding to wall suction and injection. One must ignore negative integers to avoid self-cancellation. One can put

$$\psi_n(r,z) = (\alpha_n z + \beta_n)\sin[\tfrac{1}{2}(2n+1)\pi r^2] \quad \text{or} \quad \psi(r,z) = \sum_{n=0}^{\infty}(\alpha_n z + \beta_n)\sin[\tfrac{1}{2}(2n+1)\pi r^2] \tag{20}$$

The headwall boundary condition may be satisfied by means of orthogonality; one recovers, for an injection profile $u_0(r)$, the following compact form:

$$\beta_n = \frac{4}{(2n+1)\pi}\int_0^1 u_0(r)\cos[\left(n+\tfrac{1}{2}\right)\pi r^2]\,r\mathrm{d}r \tag{21}$$

The third condition becomes

$$\frac{\partial \psi(1,z)}{\partial z} = \sum_{n=0}^{\infty}\alpha_n \sin[(n+\tfrac{1}{2})\pi] = 1 \quad \text{or} \quad \sum_{n=0}^{\infty}(-1)^n\alpha_n = 1 \tag{22}$$

Clearly, an infinite number of possibilities exist that will, in principle, satisfy Eq. (22), depending on the behavior of α_n. One of the choices for α_n may be arrived at by optimizing the total kinetic energy in the chamber. The underlying principle projects that a flow may choose the path of least or most energy expenditure. To test this behavior, we evaluate the local kinetic energy at (r,θ,z) for each eigensolution using

$$E_L^2(r,\theta,z,n) = \tfrac{1}{2}u_n^2 = \tfrac{1}{2}(u_{r,n}^2 + u_{\theta,n}^2 + u_{z,n}^2) \tag{23}$$

where each mode is an exact solution bearing the form

$$\begin{cases} u_{r,n} = -\dfrac{\alpha_n}{r}\sin\eta \\ u_{r,\theta} = 0 \\ u_{z,n} = \pi\left(\alpha_n z + \beta_n\right)(2n+1)\cos\eta \end{cases} ; \quad \eta \equiv \tfrac{1}{2}(2n+1)\pi r^2 \tag{24}$$

By assuming a system of eigensolutions with individual kinetic energies, their cumulative energy can be written locally as

$$E_L^2 = \sum_{n=0}^{\infty} E_L^2(r,\theta,z,n) = \tfrac{1}{2}\sum_{n=0}^{\infty}\left[\alpha_n^2 r^{-2}\sin^2\eta + \pi^2\left(\alpha_n z + \beta_n\right)^2 (2n+1)^2\cos^2\eta\right] \tag{25}$$

The total kinetic energy in the chamber volume V may be calculated by integrating the local kinetic energy over the length and chamber cross-section. One puts

$$E_V^2 = \int_0^{2\pi}\int_0^L\int_0^1 E_L^2 \, r\mathrm{d}r\mathrm{d}z\mathrm{d}\theta = \pi\sum_{n=0}^{\infty}\int_0^L\int_0^1\left[\alpha_n^2 r^{-2}\sin^2\eta + \pi^2\left(z\alpha_n + \beta_n\right)^2(2n+1)^2\cos^2\eta\right]r\mathrm{d}r\mathrm{d}z \tag{26}$$

Straightforward evaluation and simplification over the chamber volume yields

$$E_V^2 = \tfrac{1}{12}\pi^3 L^3 \sum_{n=0}^{\infty}\left(\alpha_n^2 a_n + \alpha_n L^{-1} b_n + L^{-2} c_n + \alpha_n^2 \pi^{-2} L^{-2} d_n\right) \tag{27}$$

with

$$\begin{cases} a_n = (2n+1)^2; \quad b_n = 3\beta_n a_n; \quad c_n = 3\beta_n^2 a_n \\ d_n = 3\{\mathcal{E} + \ln[(2n+1)\pi] - \mathrm{Ci}[(2n+1)\pi]\} \end{cases} \tag{28}$$

Here $\mathcal{E} \simeq 0.577216$ is Euler's Gamma constant. At this point, one may seek the extremum of the total kinetic energy subject to the fundamental constraint

$$\sum_{n=0}^{\infty}(-1)^n \alpha_n = 1 \quad \text{(constant radial velocity from sidewall injection)} \tag{29}$$

To make further headway, the method of Lagrangian multipliers may be conveniently employed by first defining the constrained energy function

$$g = E_V^2 + \lambda\left[\sum_{i=0}^{\infty}(-1)^i \alpha_i - 1\right] \tag{30}$$

Equation (27) can then be maximized or minimized by imposing $\nabla g(\alpha_0, \alpha_1, \alpha_2, ..., \ldots, \lambda) = 0$. In shorthand notation, one puts

$$\nabla g(\alpha_i, \lambda) = 0 \quad i = \{0, 1, 2..., \infty\} \tag{31}$$

Subsequently, the constrained energy function may be differentiated with respect to each of its variables to obtain

$$\frac{\partial g}{\partial \alpha_i} = \tfrac{1}{12}\pi^3 L^3\left(2\alpha_i a_i + L^{-1} b_i + 2\alpha_i \pi^{-2} L^{-2} d_i\right) + (-1)^i \lambda = 0; \quad i = \{0, 1, 2..., \infty\} \tag{32}$$

$$\frac{\partial g}{\partial \lambda} = \sum_{i=0}^{\infty}(-1)^i \alpha_i - 1 = 0 \tag{33}$$

Equation (32) can be solved for α_i in terms of λ such that

$$\alpha_i = -\frac{6(-1)^i \lambda + \tfrac{1}{2} b_i \pi^3 L^2}{\pi^3 L^3 (a_i + \pi^{-2} L^{-2} d_i)} \tag{34}$$

The outcome can be suitably substituted into Eq. (33) to retrieve

$$\lambda = -\frac{2\pi^3 L^3 + \pi^3 L^2 \sum_{i=0}^{\infty}(-1)^i b_i (a_i + \pi^{-2} L^{-2} d_i)^{-1}}{12\sum_{i=0}^{\infty}(a_i + \pi^{-2} L^{-2} d_i)^{-1}} \tag{35}$$

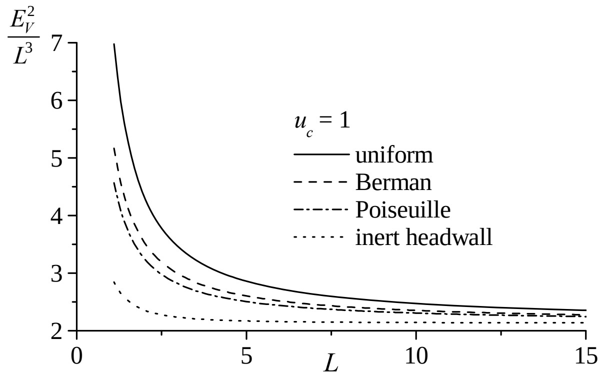

Figure 2. Variation of kinetic energy for each of the classic headwall injection profiles. Results are shown for a headwall-to-sidewall injection velocity ratio of unity.

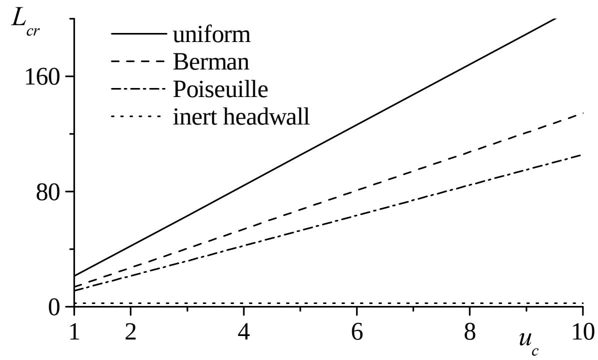

Figure 3. Critical length beyond which the energy density varies by less than 7.5% for a given headwall-to-sidewall injection velocity ratio.

When λ is inserted into Eq. (34), the general solution for α_n is obtained. In the interest of clarity, we restore the original indices and write

$$\alpha_n = \frac{2(-1)^n + (-1)^n L^{-1}\sum_{i=0}^{\infty}(-1)^i b_i (a_i + \pi^{-2}L^{-2}d_i)^{-1} - b_n L^{-1}\sum_{i=0}^{\infty}(a_i + \pi^{-2}L^{-2}d_i)^{-1}}{2(a_n + \pi^{-2}L^{-2}d_n)\sum_{i=0}^{\infty}(a_i + \pi^{-2}L^{-2}d_i)^{-1}} \tag{36}$$

With this expression at hand, the total energy given by Eq. (27) is fully determined. However, given that the Taylor-Culick model is semi-infinite, it is useful to introduce a suitable form of energy density such as $\mathscr{E} = E_V^2 / L^3$. Then by plotting $\mathscr{E}$ versus L in Fig. 2, one is able to assess the energy requirements associated with several standard headwall injection profiles. It can thus be seen that the headwall injection profiles that are accompanied by the most kinetic energy are, in descending order, the uniform, Berman (half-cosine), and Poiseuille solutions. One also finds that as the length of the chamber is increased at fixed radius, $\mathscr{E}$ approaches a constant asymptotic value of $\mathscr{E}_\infty = 2\pi/3 \simeq 2.0944$, for each of the headwall injection patterns. A critical aspect ratio L_{cr} can therefore be conceived beyond which the kinetic energy will vary by less than 7.5% from its final asymptotic value $\mathscr{E}_\infty$. The choice of a 7.5% variation is dictated by the slow monotonic decay of the kinetic energy density function shown in Fig. 2. Whereas the slope slips to 1% rather rapidly, its progression to the asymptotic value is exceedingly slow. Forthwith, a graph of L_{cr} is provided in Fig. 3 as function of the headwall-to-sidewall injection velocity ratio, u_c. Here too, the largest L_{cr} corresponds to the uniform profile and is followed by Berman's and Poiseuille's. For a chamber with $L \ge L_{cr}$, one may safely assume an infinitely long chamber in evaluating Eq. (36), thereby achieving a substantial reduction in complexity. In practice, when the headwall injection velocity is of order unity, as in the case of solid rocket motors (SRMs), the critical aspect ratio is relatively low. For example, using $u_c = 1, \frac{1}{2}\pi, 2$ (i.e. assuming that headwall and sidewall grain surfaces are burning at equal rates, so that $U_c = U_w$) L_{cr} can be calculated to be 21.3, 27.1, and 21.4 for the uniform, Berman, and Poiseuille solutions, respectively. Because the aspect ratio of most SRMs exceeds 20, the large *L* approximation may be safely used for simulated SRMs.

B. Large *L* Approximation

A simple case may be illustrated for a simulated rocket chamber with an aspect ratio that exceeds L_{cr}. Letting $L \to \infty$, Eq. (36) reduces to

$$\alpha_n = (-1)^n \left(a_n \sum_{i=0}^{\infty} a_i^{-1} \right)^{-1} = \frac{8(-1)^n}{\pi^2 (2n+1)^2} \tag{37}$$

This simple relation identically satisfies the fundamental constraint expressed through Eq. (29). More importantly, Eq. (37) establishes that for long chambers, $\{\alpha_n\}$ becomes independent of the headwall injection sequence $\{\beta_n\}$. This grants $\{\alpha_n\}$ a universal character, namely, specificity that is independent of the imposed fore-end profile. In actuality, the cancellation of the role of u_0 may be physically explained. Firstly, as confirmed in two former studies that consider similar solutions driven by arbitrary headwall injection,[15,35] the influence of u_0 diminishes in the downstream direction. It thus becomes negligible in sufficiently long chambers. Secondly, at its most fundamental level, the Taylor-Culick model is driven by sidewall injection. Suppressing sidewall injection will drastically change the character of the solution, whereas suppressing headwall injection does not.[16] So while sidewall injection gives rise to the primary stream, headwall mass addition constitutes a secondary contribution. Thirdly, flow steepening or flattening can occur in the absence of headwall injection, having been reported in chambers in which only sidewall injection is present.

C. Least Kinetic Energy Solution

It should be noted that the optimization technique based on Lagrangian multipliers enables us to identify the problem's extremum with no first-hand indication of whether the outcome corresponds to a minimum or a maximum. Nonetheless, a simple substitution of Eq. (37) into Eq. (27) provides a straightforward platform for comparing the energy content of the present approximation to that of Taylor-Culick's. We find that the strategy just pursued exposes the solution that is accompanied by the least kinetic energy. For the inert headwall case, the energy-minimized formulation that emerges from Eq. (20) collapses into

$$\psi(r,z) = \frac{8}{\pi^2} z \sum_{n=0}^{\infty} \frac{(-1)^n}{(2n+1)^2} \sin\left[\tfrac{1}{2}(2n+1)\pi r^2\right] \tag{38}$$

where only a few terms are needed for convergence. For other injection profiles, α_n remains the same while β_n varies according to the imposed fore-end flow distribution. The stream functions and axial velocities with least kinetic energy are posted in Table 1 using four different headwall injection patterns. Other possible solutions could be just as easily obtained by direct substitution and evaluation of Eqs. (36), (21), and (20). Corresponding streamlines are illustrated in Fig. 4 for zero headwall injection as well as for uniform, Berman (half cosine), and Poiseuille configurations. Using solid lines to denote the traditional Taylor-Culick's, the steepened solutions are shown using broken lines. The energy-minimized solutions exhibit steep curvatures that are reminiscent of those associated with turbulent or compressible flow motions.[36]

D. Type I Solutions with Increasing Energy Levels

So far a Taylor-Culick type solution has been captured bearing the minimum kinetic energy that the flow may be able to sustain. If a family of solutions could be conceived with continuous or discrete/quantized energy states, then the particular solution that we have identified could be viewed as the datum, ground level, or anchor point. It would hence be valuable to identify alternative mean flow solutions that exhibit increasing levels of kinetic energy, specifically those leading to the flowfield with maximum kinetic energy. It would also be instructive to rank the Taylor-Culick solution according to its energy content within the set of possible solutions. To this end, we consider long chambers and make use of Eq. (37) as a guide. As indicated earlier, the source of steepening stems from sidewall injection, and thus the sidewall injection sequence $\{\alpha_n\}$ will comprise the key parameters that control the energy level for a given flowfield. From this standpoint, we introduce an alternative formulation for $\{\alpha_n\}$. Inspired by the form obtained through Lagrangian optimization, we note that

Table 1. Mean flow solutions with least kinetic energy for several headwall injection patterns

Headwall injection $u_0(r)$	Stream function $\psi(r,z)$	Axial velocity $u_z(r,z)$
0	$\frac{8}{\pi^2} z \sum_{n=0}^{\infty} \frac{(-1)^n}{(2n+1)^2} \sin\eta; \quad \eta = \frac{1}{2}\pi(2n+1)r^2$	$\frac{8}{\pi} z \sum_{n=0}^{\infty} \frac{(-1)^n}{(2n+1)} \cos\eta$
u_c	$\frac{4}{\pi^2}(2z+u_c) \sum_{n=0}^{\infty} \frac{(-1)^n}{(2n+1)^2} \sin\eta$	$\frac{4}{\pi}(2z+u_c) \sum_{n=0}^{\infty} \frac{(-1)^n}{(2n+1)} \cos\eta$
$u_c \cos\left(\frac{1}{2}\pi r^2\right)$	$\frac{u_c}{\pi}\sin\left(\frac{1}{2}\pi r^2\right) + \frac{8}{\pi^2} z \sum_{n=0}^{\infty} \frac{(-1)^n}{(2n+1)^2} \sin\eta$	$u_c \cos\left(\frac{1}{2}\pi r^2\right) + \frac{8}{\pi} z \sum_{n=0}^{\infty} \frac{(-1)^n}{(2n+1)} \cos\eta$
$u_c\left(1-r^2\right)$	$\frac{8}{\pi^2} \sum_{n=0}^{\infty} \frac{1}{(2n+1)^2}\left[(-1)^n z + \frac{u_c}{\pi(2n+1)}\right]\sin\eta$	$\frac{8}{\pi} \sum_{n=0}^{\infty} \frac{1}{(2n+1)}\left[(-1)^n z + \frac{u_c}{\pi(2n+1)}\right]\cos\eta$

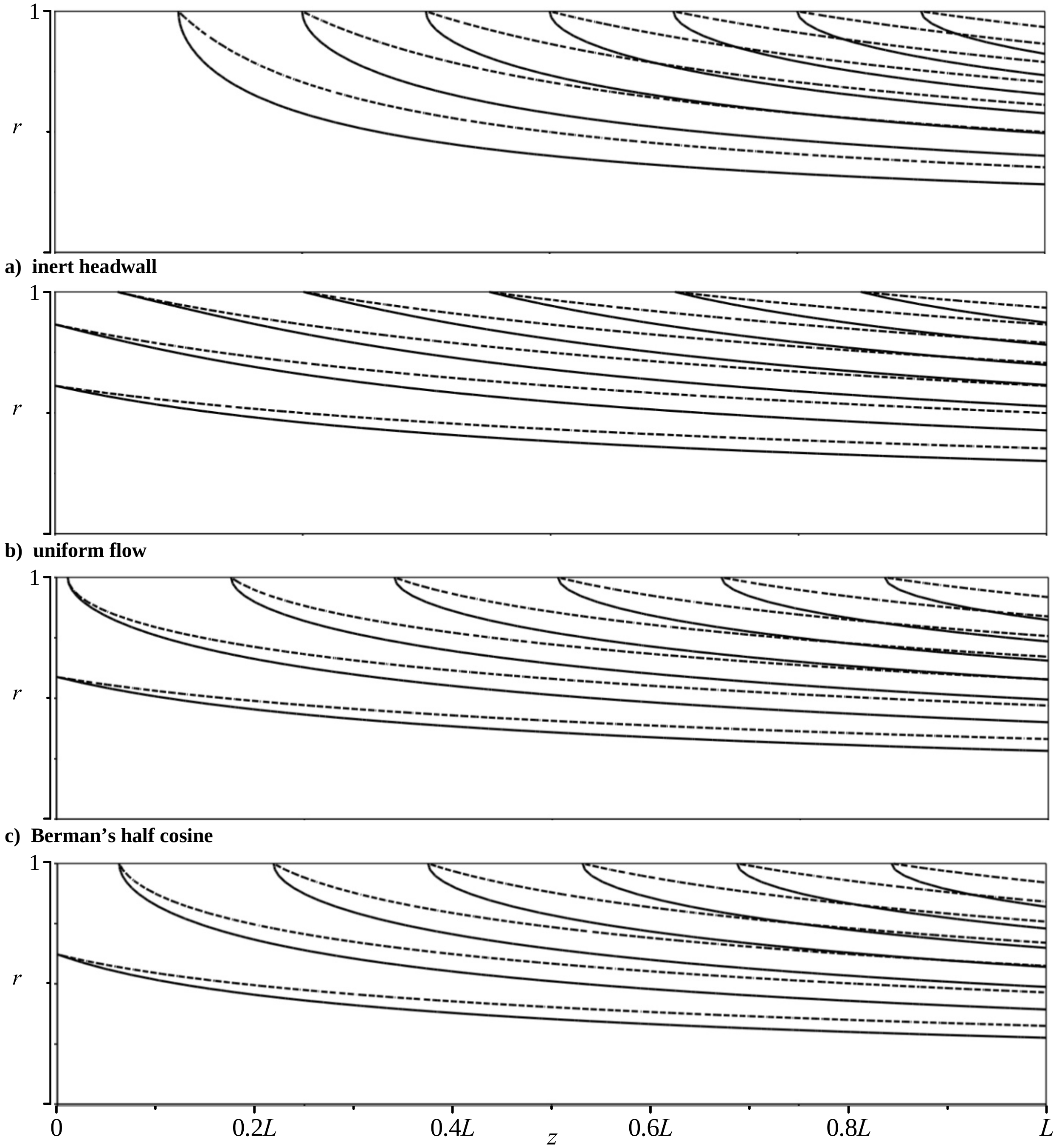

d) Poiseuille flow

Figure 4. Comparison of the Taylor-Culick (solid) streamlines and the Type I energy-minimized solution with steeper curvature (broken lines).

$$\alpha_n = \frac{8(-1)^n}{\pi^2 (2n+1)^2} \sim \frac{(-1)^n A_2}{(2n+1)^2} \tag{39}$$

where $A_2 = 8/\pi^2$ can be deduced from the radial inflow requirement given by Eq. (29). Its subscript is connected with the power of $(2n+1)$ in the denominator. To generalize, one can assume the generic Type I form

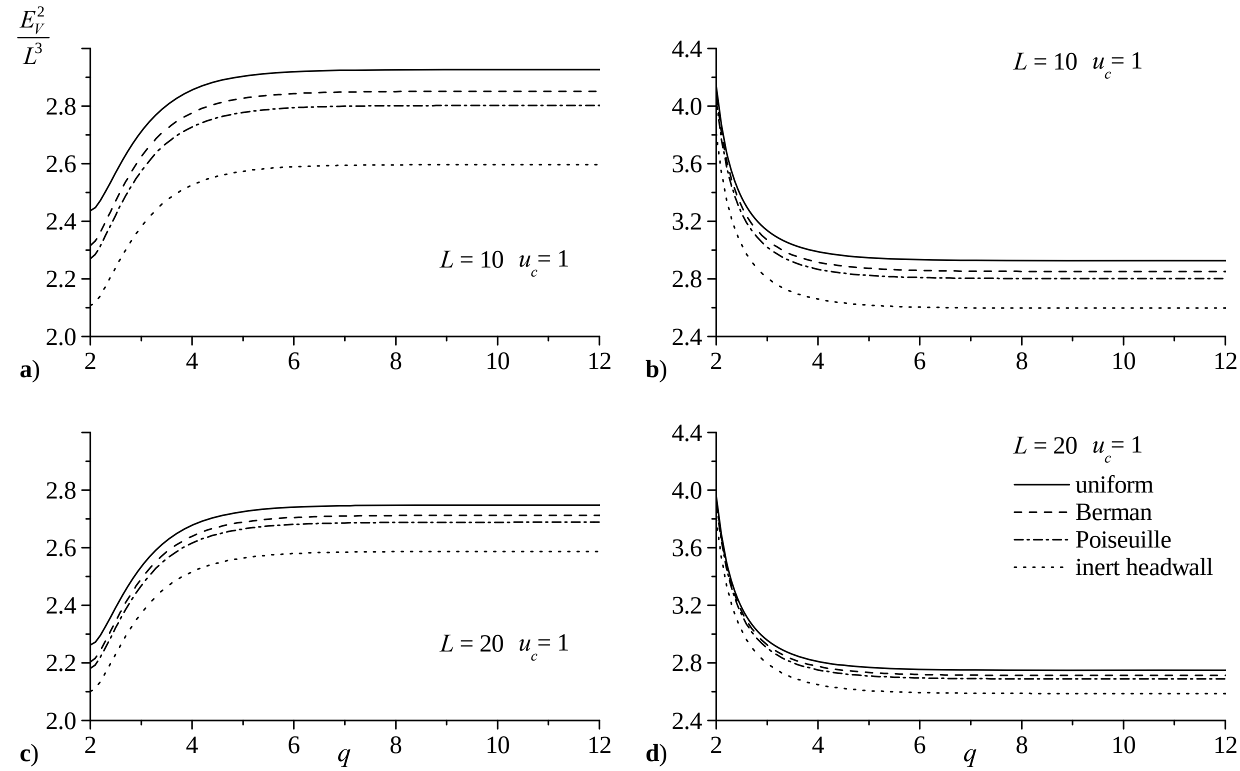

Figure 5. Total kinetic energy density in a simulated SRM chamber for either (a,c) Type I solutions (left) with increasing energy levels or (b,d) Type II solutions (right) with decreasing energy levels. Results are for *L* = 10 and 20.

$$\alpha_n^-(q) = \frac{(-1)^n A_q}{(2n+1)^q}; \quad q \geq 2 \tag{40}$$

where $q = 2$ reproduces the state of least energy expenditure. This relation will be made to satisfy Eq. (29) when

$$\sum_{n=0}^{\infty} (-1)^n \frac{(-1)^n A_q}{(2n+1)^q} = 1 \quad \text{or} \quad A_q = \frac{1}{\sum_{n=0}^{\infty} (2n+1)^{-q}} = \frac{1}{\zeta(q)(1-2^{-q})}; \quad \zeta(q) = \sum_{k=1}^{\infty} k^{-q} \tag{41}$$

where ζ is Riemann's zeta function. Note that the $q \geq 2$ condition is needed to ensure series convergence. Backward substitution enables us to collect the proper form of α_n, namely,

$$\alpha_n^-(q) = \frac{(-1)^n}{(2n+1)^q \sum_{k=0}^{\infty} (2k+1)^{-q}} = \frac{(-1)^n}{\zeta(q)(1-2^{-q})(2n+1)^q}; \quad q \geq 2 \quad \text{(Type I)} \tag{42}$$

The exponent q may be dubbed the *kinetic energy power index*. With the form given by Eq. (42), one can plot the variation of the total kinetic energy versus the kinetic energy power index q. This plot is shown in Fig. 5a for zero headwall injection. Interestingly, as $q \to \infty$, Taylor-Culick's classic solution is strictly recovered. In fact, using Eq. (42), it can be rigorously demonstrated that

$$\lim_{q \to \infty} \alpha_n^-(q) = \begin{cases} 1; & n = 0 \\ 0; & \text{elsewhere} \end{cases} \tag{43}$$

This result identically reproduces Taylor-Culick's expression. All of the Type I formulations that can be precipitated from Eq. (42) possess kinetic energies that are lower than Taylor-Culick's. They can be bracketed between Eq. (38) and $\psi(r,z) = z\sin(\frac{1}{2}\pi r^2)$. In practice, all solutions with $q \geq 5$ will be Taylor-Culick-like as their energies will differ by less than 1%. The most distinct solutions will correspond to $q = 2$, 3, and 4 with energies that are 81.1, 91.7, and 97.3% of Taylor-Culick's.

E. Type II Solutions with Decreasing Energy Levels

To capture solutions with energies that exceed that of Taylor-Culick's, a modified formulation for α_n is in order. One may set

$$\alpha_n^+(q) = \frac{B_q}{(2n+1)^q}; \quad q \ge 2 \tag{44}$$

The key difference here stands in the exclusion of the $(-1)^n$ multiplier which was previously retained in Eq. (40). Unless this term is lumped into B_q, no solutions can be captured with higher energies than Taylor-Culick's. The remaining steps follow similar lines as before. Substitution into Eq. (29) unravels

$$\sum_{n=0}^{\infty}(-1)^n \frac{B_q}{(2n+1)^q} = 1 \quad \text{or} \quad B_q = \frac{1}{\sum_{n=0}^{\infty}(-1)^n (2n+1)^{-q}} = \frac{4^q}{\zeta(q,\frac{1}{4}) - \zeta(q,\frac{3}{4})} \tag{45}$$

where $\zeta(q,x)$ is the generalized Riemann zeta function. Equation (45) enables us to retrieve

$$\alpha_n^+(q) = \frac{(2n+1)^{-q}}{\sum_{k=0}^{\infty}(-1)^k (2k+1)^{-q}} = \frac{4^q (2n+1)^{-q}}{\zeta(q,\frac{1}{4}) - \zeta(q,\frac{3}{4})} \quad \text{(Type II)} \tag{46}$$

It can be shown that all Type II solutions emerging from Eq. (46) dispose of higher kinetic energies than Taylor-Culick's. The variation of the solution with respect to q is illustrated in Fig. 5b. According to this form of $\{\alpha_n^-\}$, Taylor-Culick's model is recoverable asymptotically by taking the limit as $q \to \infty$. Here too, most of the solutions will exhibit energies that lie within 1% of Taylor-Culick's. The most interesting solutions are, in descending order, those corresponding to $q = 2$, 3, and 4 with energies that are 47.0, 8.08, and 2.40% larger than Taylor-Culick's. So in view of the two types of solutions obtained heretofore, specifically with energies lagging or exceeding that of Taylor-Culick's, the latter appears to constitute a stable saddle function to which other possible forms will quickly converge when their energies are either increased or decreased.

When the energy level is fixed at $q = 2$, a simplification follows. Catalan's constant emerges in Eq. (46), namely, in the form

$$\mathscr{C} = \sum\nolimits_{k=0}^{\infty}(-1)^k (2n+1)^{-2} \simeq 0.915966 \tag{47}$$

Several Type II solutions that carry the most energy at $q = 2$ are plotted in Fig. 6 and listed in Table 2. In Fig. 6, the Type II approximations are seen to overshoot the Taylor-Culick streamline curvature for four cases corresponding to different headwall injection patterns. These cover standard configurations such as: a) inert headwall, b) uniform flow, c) Berman's half cosine, and d) Poiseuille profiles.

In Fig. 7, the least and most kinetic energy densities for $q = 2$ and either Type I or Type II solutions are compared to Taylor-Culick's energy density given several headwall injection profiles. While the highest and lowest borderlines restrict the range of physically possible excursions in energy, it is interesting that the energy density associated with Taylor-Culick's acts as a bisector, distinctly splitting the domain into low and high energy bands.

Table 2. Mean flow solutions with most kinetic energy for several headwall injection patterns

Headwall injection $u_0(r)$	Stream function $\psi(r,z)$	Axial velocity $u_z(r,z)$
0	$\frac{z}{\mathscr{C}}\sum_{n=0}^{\infty}\frac{\sin\eta}{(2n+1)^2}$	$\pi\frac{z}{\mathscr{C}}\sum_{n=0}^{\infty}\frac{\cos\eta}{(2n+1)}$
u_c	$\sum_{n=0}^{\infty}\left[\frac{z}{\mathscr{C}}+\frac{4(-1)^n}{\pi^2}u_c\right]\frac{\sin\eta}{(2n+1)^2}$	$\pi\sum_{n=0}^{\infty}\left[\frac{z}{\mathscr{C}}+\frac{4(-1)^n}{\pi^2}u_c\right]\frac{\cos\eta}{(2n+1)}$
$u_c\cos\left(\frac{1}{2}\pi r^2\right)$	$\frac{u_c}{\pi}\sin\left(\frac{1}{2}\pi r^2\right)+\frac{z}{\mathscr{C}}\sum_{n=0}^{\infty}\frac{\sin\eta}{(2n+1)^2}$	$u_c\cos\left(\frac{1}{2}\pi r^2\right)+\pi\frac{z}{\mathscr{C}}\sum_{n=0}^{\infty}\frac{\cos\eta}{(2n+1)}$
$u_c\left(1-r^2\right)$	$\sum_{n=0}^{\infty}\left[\frac{z}{\mathscr{C}}+\frac{8u_c}{\pi^3(2n+1)}\right]\frac{\sin\eta}{(2n+1)^2}$	$\pi\sum_{n=0}^{\infty}\left[\frac{z}{\mathscr{C}}+\frac{8u_c}{\pi^3(2n+1)}\right]\frac{\cos\eta}{(2n+1)}$

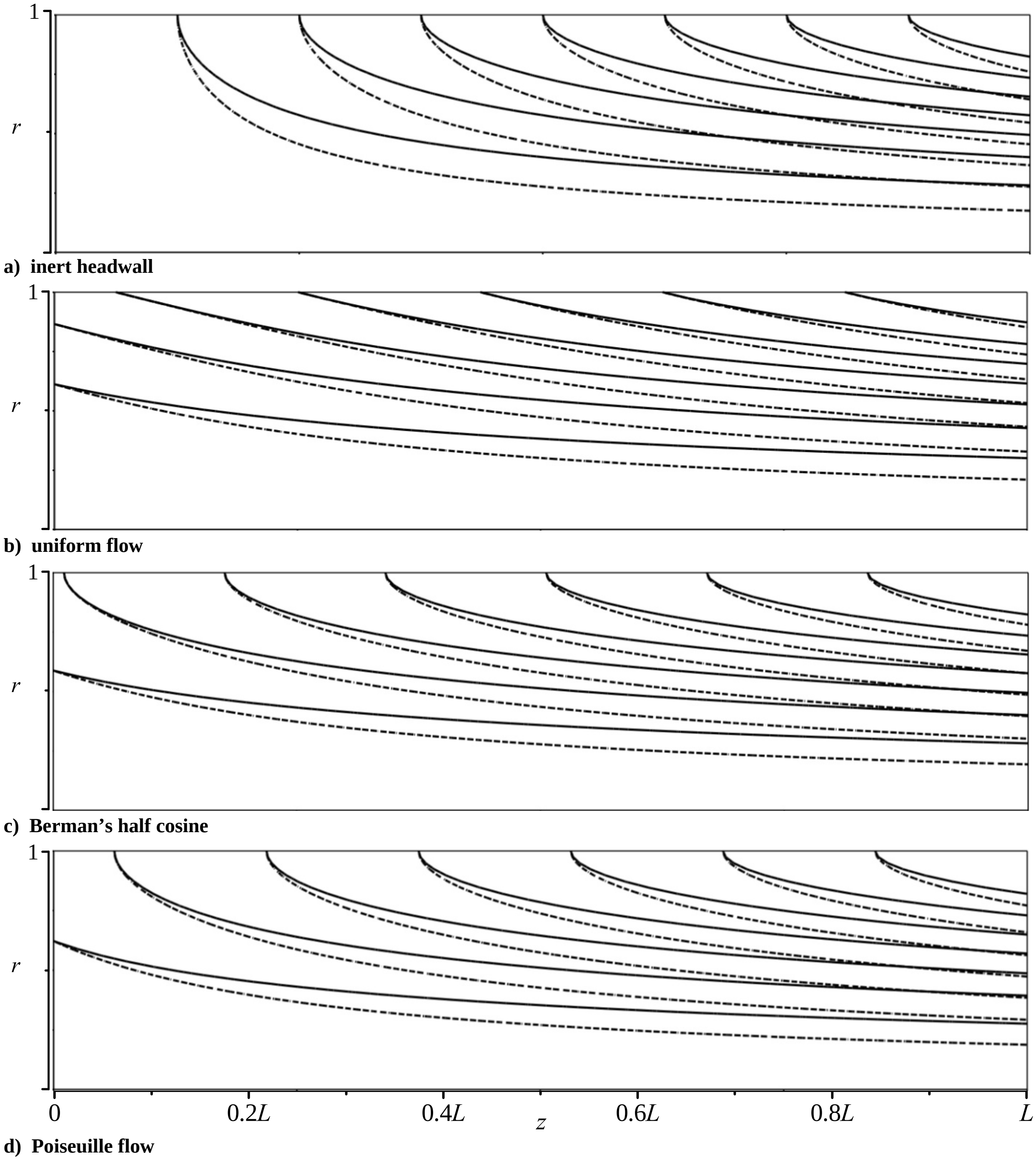

Figure 6. Comparison of the Taylor-Culick (solid) streamlines and the Type II energy-maximized Taylor-Culick solution with overshooting curvature (broken lines).

F. Vorticity

The vorticity may be determined from

$$\omega_\theta = \frac{\partial u_r}{\partial z} - \frac{\partial u_z}{\partial r} = \pi^2 r \sum_{n=0}^{\infty} (2n+1)^2 (\alpha_n z + \beta_n) \sin\eta \tag{48}$$

This expression is evaluated for the least and most kinetic energy formulations ($q = 2$), as well as for the representative injection profiles considered in this work. These are provided in Table 3.

G. Asymptotic Limits of the Kinetic Energy Density

In the large L approximation with $q = 2$, the Type II kinetic energy density $\mathscr{E}$ approaches a constant value of $\mathscr{E}_\infty = \pi^5/(96\mathscr{C}^2) \simeq 3.79944$. Note that the asymptotic value for Taylor-Culick's, $\mathscr{E}_\infty^\infty \equiv \pi^3/12 \simeq 2.5838$, is recovered as $q \to \infty$. This explains the reason for the energy bands in Fig. 7 to become more parallel at constant q as L is increased. In general, provided that u_c is finite, the limit of the kinetic energy density can be written as

$$\mathscr{E}_\infty = \tfrac{1}{12}\pi^3 \sum_{n=0}^{\infty} (2n+1)^2 \alpha_n^2 = \mathscr{E}_\infty^\infty \sum_{n=0}^{\infty} (2n+1)^2 \alpha_n^2 \tag{49}$$

For the Type I solutions, substitution of Eq. (42) yields a closed form expression, namely,

$$\mathscr{E}_\infty^-(q) = \mathscr{E}_\infty^\infty \left[\sum_{k=0}^{\infty} (2k+1)^{-q} \right]^{-2} \sum_{n=0}^{\infty} (2n+1)^{2-2q} = \mathscr{E}_\infty^\infty \frac{4^q - 4}{(2^q - 1)^2} \frac{\zeta(2q-2)}{[\zeta(q)]^2} \tag{50}$$

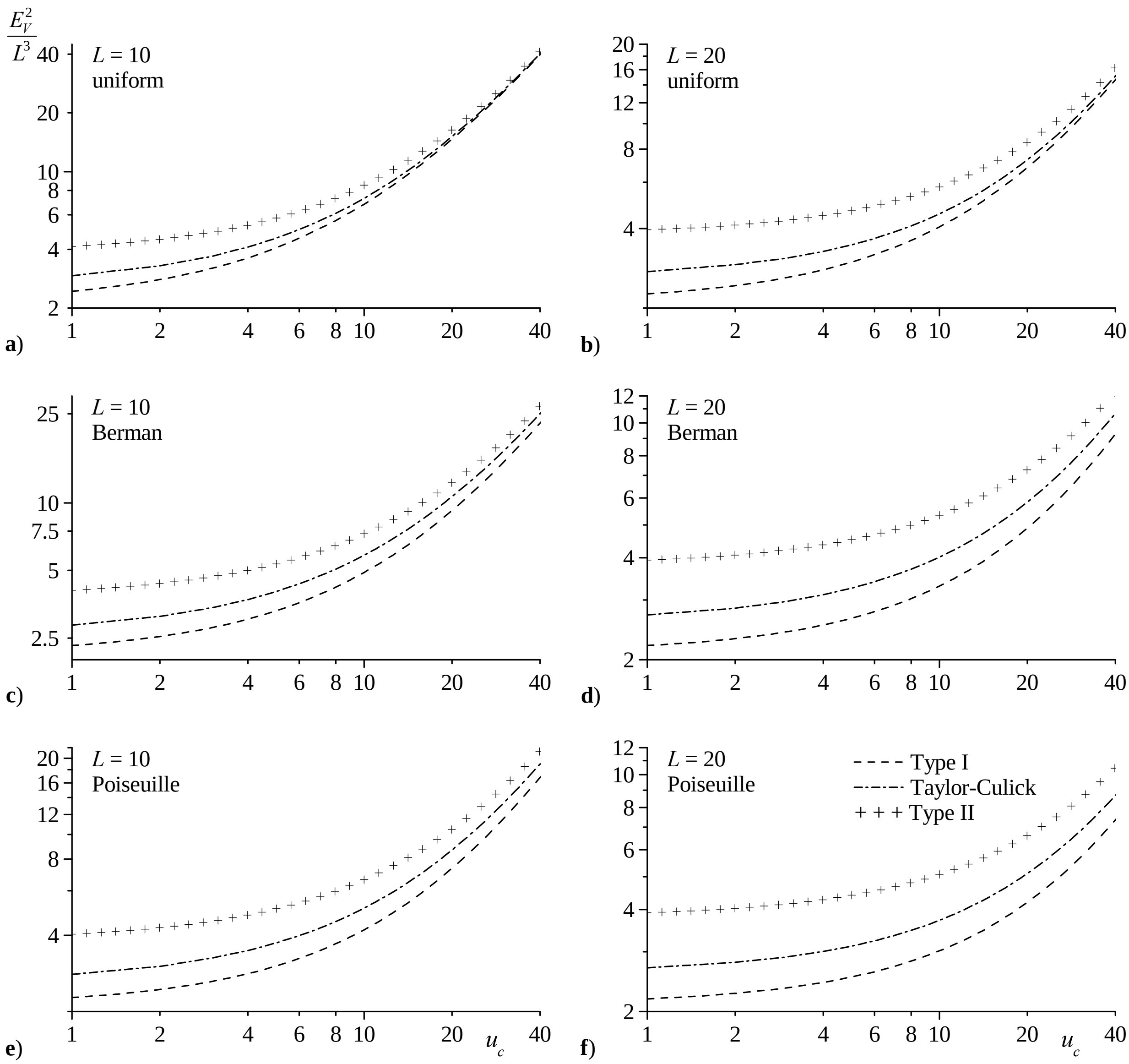

Figure 7. Total kinetic energy density for Type I and Type II solutions tailing and leading Taylor-Culick's. Results are for *L* = 10 (left) and 20 (right) given: (a,b) uniform, (c,d) Berman, and (e,f) Poiseuille headwall injection profiles.

Table 3. Vorticity with least or most kinetic energy for several headwall injection patterns

Headwall injection $u_0(r)$	Type I vorticity $\omega_\theta^-(r,z)$	Type II vorticity $\omega_\theta^+(r,z)$
0	$8rz\sum_{n=0}^{\infty}(-1)^n\sin\eta$	$\frac{\pi^2}{\mathscr{C}}rz\sum_{n=0}^{\infty}(-1)^n\sin\eta$
u_c	$4(z+u_c)r\sum_{n=0}^{\infty}2(-1)^n\sin\eta$	$r\sum_{n=0}^{\infty}\left[\frac{\pi^2}{\mathscr{C}}z+4(-1)^n u_c\right]\sin\eta$
$u_c\cos\left(\frac{1}{2}\pi r^2\right)$	$\pi u_c r\sin\left(\frac{1}{2}\pi r^2\right)+8rz\sum_{n=0}^{\infty}(-1)^n\sin\eta$	$\pi u_c r\sin\left(\frac{1}{2}\pi r^2\right)+\frac{\pi^2}{\mathscr{C}}rz\sum_{n=0}^{\infty}\sin\eta$
$u_c\left(1-r^2\right)$	$8r\sum_{n=0}^{\infty}\left[(-1)^n z+\frac{u_c}{\pi(2n+1)}\right]\sin\eta$	$r\sum_{n=0}^{\infty}\left[\frac{\pi^2}{\mathscr{C}}z+\frac{8u_c}{\pi(2n+1)}\right]\sin\eta$

In like manner, for the Type II solutions, Eq. (46) leads to

$$\mathscr{E}_\infty^+(q)=\mathscr{E}_\infty^\infty\left[\sum_{k=0}^{\infty}(-1)^k(2k+1)^{-q}\right]^{-2}\sum_{n=0}^{\infty}(2n+1)^{2-2q}=\mathscr{E}_\infty^\infty\frac{4^q(4^q-4)\zeta(2q-2)}{[\zeta(q,\frac{1}{4})-\zeta(q,\frac{3}{4})]^2} \quad (51)$$

It is interesting to note that these asymptotic limits are independent of headwall injection (u_c or β_n). Specific values of these limits are $\mathscr{E}_\infty^-(2)=2\pi/3\simeq 2.0944$, $\mathscr{E}_\infty^-(4)=4\pi/5\simeq 2.5133$, and $\mathscr{E}_\infty^-(6)=155\pi/189\simeq 2.5764$ for the Type I, and $\mathscr{E}_\infty^+(2)\simeq 3.7994$, $\mathscr{E}_\infty^+(4)\simeq 2.6457$, and $\mathscr{E}_\infty^+(6)\simeq 2.5907$ for the Type II. Both types approach $\mathscr{E}_\infty^\infty$ either from below or above. Since these limits are quickly achieved as the length of the chamber is increased, they are directly applicable to simulated rocket motor flows. The energy associated with each kinetic energy power index may be inferred from Fig. 8 below. Note that the Taylor-Culick limit of 2.5838 is practically reached by both Type I and Type II solutions with differences of less than 0.287 and 0.265% at $q=6$. Given the maximum range at $q=2$, the total allowable excursion in energy that the mean flow can undergo may be readily estimated at $\left[\mathscr{E}_\infty^+(2)-\mathscr{E}_\infty^-(2)\right]/\mathscr{E}_\infty^\infty=66\%$, an appreciable portion of the available energy.

IV. Conclusions

In the past four decades, the Taylor-Culick solution with impermeable headwall has been extensively used in the propulsion community. Recently, an extended form has been presented in which variable headwall injection could be accommodated.[17,37] In this article, we show that for each type of headwall injection pattern and chamber aspect ratio, other solutions may be obtained, and these are accompanied by lower or higher kinetic energies that vary by up to 66% of their mean value. After identifying that $\alpha_n^-\sim(-1)^n(2n+1)^{-2}$ yields the profile with least kinetic energy, similar (Type I) solutions are unraveled in ascending order, $\alpha_n^-\sim(-1)^n(2n+1)^{-q}$; $q>2$, up to Taylor-Culick's. The latter is asymptotically recovered in the limit as $q\to\infty$. In practice, however, most solutions become indiscernible from Taylor-Culick's for $q\geq 5$. Interestingly, those obtained with $q=2$, 3, and 4 exhibit energies that are 18.9, 8.28 and 2.73% lower than their remaining counterparts. When the same analysis is repeated using $\alpha_n^+\sim(2n+1)^{-q}$; $q\geq 2$, a complementary family of (Type II) solutions is identified with descending energy levels. Their most notable profiles correspond to $q=2$, 3, and 4 with energies that are 47.0, 8.08, and 2.40% higher than Taylor-Culick's. Here too, all Type II solutions resemble the classic form which is identically regained as $q\to\infty$. Effectively, both Type I and II solutions converge to the Taylor-Culick representation when their

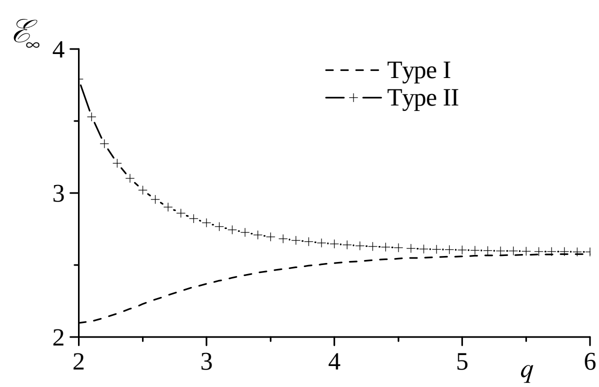

Figure 8. Asymptotic limits of the kinetic energy density for large *L* showing rapid convergence of both Type I and Type II solutions to Taylor-Culick's value of 2.5838.

energies are reduced or augmented, respectively. Profiles belonging to these families of solutions with $q \to \infty$ and $u_c = 1, \frac{1}{2}\pi, 2$ (corresponding to uniform, Berman, and Poiseuille injection) have been verified in separate work by the authors[37] using computational fluid dynamics. Additional experimental validation is hoped to be achieved from sensitive test measurements that utilize modern instrumentation.

The generation of blunter or smoother profiles with decreasing or increasing chamber energy can have important implications on combustion instability analysis. Such behavior can be used to explain why the mean flow can be blunter or steeper during acoustic wave growth. It may also be used to institute a meaningful theory to capture the inevitable two-way coupling that exists between the bulk gaseous motion and the unsteady wave disturbances. As a windfall, it may be used to explain the increased mean pressure (DC shift) during acoustic energy amplification and cascading. A plausible hypothesis is this: as unsteady energy seeks to escape from a rocket chamber or combustor, transfer to the mean flow will immediately constitute one of the possible avenues by which acoustic energy may be expended, thus leading to a dynamic energy exchange between the steady and unsteady flowfields. In the past, such an avenue has not been considered. In practice, both fields, not only the unsteady waves, can alter character and absorb or release energy. The energy transferred from the unsteady waves to the mean flow can, under one scenario, increase the wall shear stress, grain regression, mass addition, and the engendered mean pressure shift.

Acknowledgments

This work is sponsored by the National Science Foundation. The first author wishes to acknowledge valuable discussions with Dr. Grégoire Casalis, Professor and Director of the Doctoral School of Aeronautics and Astronautics, SUPAERO, and Research Director, Department of Aerodynamics and Energetics, ONERA, Toulouse, France.

References

[1]Majdalani, J., "Physicality of Core Flow Models in Rocket Motors," *Journal of Propulsion and Power,* Vol. 19, No. 1, 2003, pp. 156-159.

[2]Majdalani, J., Flandro, G. A., and Fischbach, S. R., "Some Rotational Corrections to the Acoustic Energy Equation in Injection-Driven Enclosures," *Physics of Fluids,* Vol. 17, No. 7, 2005, pp. 0741021-20.

[3]Fischbach, S. R., Majdalani, J., and Flandro, G. A., "Acoustic Instability of the Slab Rocket Motor," *Journal of Propulsion and Power,* Vol. 23, No. 1, 2007, pp. 146-157.

[4]Majdalani, J., Fischbach, S. R., and Flandro, G. A., "Improved Energy Normalization Function in Rocket Motor Stability Calculations," *Journal of Aerospace Science and Technology,* Vol. 10, No. 6, 2006, pp. 495-500.

[5]Majdalani, J., and Flandro, G. A., "The Oscillatory Pipe Flow with Arbitrary Wall Injection," *Proceedings of the Royal Society, Series A,* Vol. 458, No. 2022, 2002, pp. 1621-1651.

[6]Féraille, T., and Casalis, G., "Channel Flow Induced by Wall Injection of Fluid and Particles," *Physics of Fluids,* Vol. 15, No. 2, 2003, pp. 348-360.

[7]Féraille, T., Casalis, G., and Dupays, J., "Particle Effects on Solid-Propellant Motors Flow Stability," AIAA Paper 2002-3611, July 2002.

[8]Najjar, F. M., Haselbacher, A., Ferry, J. P., Wasistho, B., Balachandar, S., and Moser, R., "Large-Scale Multiphase Large-Eddy Simulation of Flows in Solid-Rocket Motors," AIAA Paper 2003-3700, June 2003.

[9]Najjar, F. M., Ferry, J. P., Haselbacher, A., and Balachandar, S., "Multiphase Flow Simulations in Alumnized Solid-Propellant Rocket Motors: Effects of Injected Agglomerate Droplet Size Distribution," *Journal of Spacecraft and Rockets,* Vol. 43, No. 6, 2006, pp. 1258-1270.

[10]Balachandar, S., Buckmaster, J. D., and Short, M., "The Generation of Axial Vorticity in Solid-Propellant Rocket-Motor Flows," *Journal of Fluid Mechanics,* Vol. 429, No. 1, 2001, pp. 283-305.

[11]Chu, W.-W., Yang, V., and Majdalani, J., "Premixed Flame Response to Acoustic Waves in a Porous-Walled Chamber with Surface Mass Injection," *Combustion and Flame,* Vol. 133, No. 6129, 2003, pp. 359-370.

[12]Chedevergne, F., Casalis, G., and Majdalani, J., "Biglobal Linear Stability Analysis and DNS Investigation of the Flow Induced by Wall Injection," AIAA Paper 2007-5796, July 2007.

[13]Culick, F. E. C., "Rotational Axisymmetric Mean Flow and Damping of Acoustic Waves in a Solid Propellant Rocket," *AIAA Journal,* Vol. 4, No. 8, 1966, pp. 1462-1464.

[14]Majdalani, J., Vyas, A. B., and Flandro, G. A., "Higher Mean-Flow Approximation for a Solid Rocket Motor with Radially Regressing Walls," *AIAA Journal,* Vol. 40, No. 9, 2002, pp. 1780-1788.

[15]Majdalani, J., "The Taylor-Culick Profile with Uniform Headwall Injection," AIAA Paper 2005-4534, July 2005.

[16]Majdalani, J., and Vyas, A. B., "Inviscid Models of the Classic Hybrid Rocket," AIAA Paper 2004-3474, July 2004.

[17]Majdalani, J., "Analytical Models for Hybrid Rockets," *Fundamentals of Hybrid Rocket Combustion and Propulsion*, edited by K. Kuo and M. J. Chiaverini, AIAA Progress in Astronautics and Aeronautics, Washington, DC, 2007, pp. 207-246.

[18]Baum, J. D., Levine, J. N., and Lovine, R. L., "Pulsed Instabilities in Rocket Motors: A Comparison between Predictions and Experiments," *Journal of Propulsion and Power,* Vol. 4, No. 4, 1988, pp. 308-316.

[19]Sabnis, J. S., Gibeling, H. J., and McDonald, H., "Navier-Stokes Analysis of Solid Propellant Rocket Motor Internal Flows," *Journal of Propulsion and Power,* Vol. 5, No. 6, 1989, pp. 657-664.

[20]Dunlap, R., Willoughby, P. G., and Hermsen, R. W., "Flowfield in the Combustion Chamber of a Solid Propellant Rocket Motor," *AIAA Journal,* Vol. 12, No. 10, 1974, pp. 1440-1445.

[21]Dunlap, R., Blackner, A. M., Waugh, R. C., Brown, R. S., and Willoughby, P. G., "Internal Flow Field Studies in a Simulated Cylindrical Port Rocket Chamber," *Journal of Propulsion and Power,* Vol. 6, No. 6, 1990, pp. 690-704.

[22]Yamada, K., Goto, M., and Ishikawa, N., "Simulative Study of the Erosive Burning of Solid Rocket Motors," *AIAA Journal,* Vol. 14, No. 9, 1976, pp. 1170-1176.

[23]Zhou, C., and Majdalani, J., "Inner and Outer Solutions for the Injection Driven Channel Flow with Retractable Walls," AIAA Paper 2003-3728, June 2003.

[24]Zhou, C., and Majdalani, J., "Improved Mean Flow Solution for Slab Rocket Motors with Regressing Walls," *Journal of Propulsion and Power,* Vol. 18, No. 3, 2002, pp. 703-711.

[25]Kurdyumov, V. N., "Steady Flows in the Slender, Noncircular, Combustion Chambers of Solid Propellants Rockets," *AIAA Journal,* Vol. 44, No. 12, 2006, pp. 2979-2986.

[26]Apte, S., and Yang, V., "Effect of Acoustic Oscillation on Flow Development in a Simulated Nozzleless Rocket Motor," *Solid Propellant Chemistry, Combustion, and Motor Interior Ballistics*, Vol. 185, edited by V. Yang, T. B. Brill, and W.-Z. Ren, AIAA Progress in Astronautics and Aeronautics, Washington, DC, 2000, pp. 791-822.

[27]Avalon, G., Casalis, G., and Griffond, J., "Flow Instabilities and Acoustic Resonance of Channels with Wall Injection," AIAA Paper 98-3218, July 1998.

[28]Griffond, J., Casalis, G., and Pineau, J.-P., "Spatial Instability of Flow in a Semiinfinite Cylinder with Fluid Injection through Its Porous Walls," *European Journal of Mechanics B/Fluids,* Vol. 19, No. 1, 2000, pp. 69-87.

[29]Casalis, G., Avalon, G., and Pineau, J.-P., "Spatial Instability of Planar Channel Flow with Fluid Injection through Porous Walls," *Physics of Fluids,* Vol. 10, No. 10, 1998, pp. 2558-2568.

[30]Griffond, J., and Casalis, G., "On the Nonparallel Stability of the Injection Induced Two-Dimensional Taylor Flow," *Physics of Fluids,* Vol. 13, No. 6, 2001, pp. 1635-1644.

[31]Griffond, J., and Casalis, G., "On the Dependence on the Formulation of Some Nonparallel Stability Approaches Applied to the Taylor Flow," *Physics of Fluids,* Vol. 12, No. 2, 2000, pp. 466-468.

[32]Ugurtas, B., Avalon, G., Lupoglazoff, N., Vuillot, F., and Casalis, G., "Stability and Acoustic Resonance of Internal Flows Generated by Side Injection," *Solid Propellant Chemistry, Combustion, and Motor Interior Ballistics*, Vol. 185, edited by V. Yang, T. B. Brill, and W.-Z. Ren, AIAA Progress in Astronautics and Aeronautics, Washington, DC, 2000, pp. 823-836.

[33]Chedevergne, F., Casalis, G., and Féraille, T., "Biglobal Linear Stability Analysis of the Flow Induced by Wall Injection," *Physics of Fluids,* Vol. 18, No. 1, 2006, pp. 014103-14.

[34]Majdalani, J., "On Steady Rotational High Speed Flows: The Compressible Taylor-Culick Profile," *Proceedings of the Royal Society, Series A,* Vol. 463, No. 2077, 2007, pp. 131-162.

[35]Saad, T., and Majdalani, J., "The Taylor Profile in Porous Channels with Arbitrary Headwall Injection," AIAA Paper 2007-4120, June 2007.

[36]Majdalani, J., "The Compressible Taylor-Culick Flow," AIAA Paper 2005-3542, July 2005.

[37]Majdalani, J., and Saad, T., "The Taylor-Culick Profile with Arbitrary Headwall Injection," *Physics of Fluids,* Vol. 19, No. 6, 2007.